



# Effect of heat treatments on microstructure and mechanical properties of sand cast Al–2Li–2Cu–0.5Mg–0.2Sc–0.2Zr alloy

Jin-shuo ZHANG, Xiao-xiang ZHONG, Liang ZHANG, Guo-hua WU, Wen-cai LIU

National Engineering Research Center of Light Alloy Net Forming and State Key Laboratory of Metal Matrix Composites, School of Materials Science and Engineering, Shanghai Jiao Tong University, Shanghai 200240, China

Received 21 April 2021; accepted 11 October 2021

**Abstract:** This study focused on modifying heat treatment schemes to enhance the mechanical properties of sand cast Al–2Li–2Cu–0.5Mg–0.2Sc–0.2Zr alloy. Different three-stage solution treatment schemes ((460 °C, 32 h) + (520 °C, 24 h) + (530/540/550 °C, 4/12/24/32 h)) and aging temperatures (125, 175, 225 °C) were designed for comparison. The microstructure evolutions were analyzed by optical microscopy (OM), scanning electron microscopy (SEM) and transmission electron microscopy (TEM). The results showed that the three-stage solution treatment of (460 °C, 32 h) + (520 °C, 24 h) + (530 °C, 12 h) could dissolve most of the secondary phases. The TEM results illustrated that fine  $\delta'$ (Al<sub>3</sub>Li) particles were homogeneously distributed in the matrix after aging at 175 °C for 8 h, accompanied by a small amount of lath-shaped  $S'$ (Al<sub>2</sub>CuMg) and plate-like  $T_1$ (Al<sub>2</sub>CuLi) phases. The best comprehensive properties of yield strength of 376 MPa, ultimate tensile strength of 458 MPa and elongation of 4.1% were obtained by the optimal heat treatment scheme ((460 °C, 32 h) + (520 °C, 24 h) + (530 °C, 12 h) + (175 °C, 8 h)).

**Key words:** Al–Li–Cu alloys; sand-casting; heat treatment; precipitation; microstructure; mechanical properties

## 1 Introduction

Since the energy crisis broke out in the 1970s, lithium-containing Al alloys have been put forward in the fields of military, aerospace and commercial applications for their good combination of low density, high specific strength and high stiffness [1–3]. The increasing content of Li could simultaneously decrease the density and increase the stiffness of aluminum, whilst several detrimental factors also appear, such as anisotropy and brittleness [4,5].

Micro-alloying elements and optimal heat treatment have been evidenced as the most effective way to develop high-performance cast Al–Li–Cu alloys [6–8]. Especially, the effect of Mg-alloying on the precipitation and hardening behavior is

dramatic. Some researchers illustrated that because of the high Mg–Cu–vacancy and Mg–Li binding energy, the precipitation of  $S'$ (Al<sub>2</sub>CuMg) and  $T_1$ (Al<sub>2</sub>CuLi) phases was strongly promoted [9–11].  $T_1$  phase, nucleating on {111} matrix planes [12], is widely accepted to be the most effective strengthening phase among the Cu-containing phases. Meanwhile, the dispersed and homogeneous  $S'$  phase is beneficial to both strength and ductility [6,13]. However, an overmuch amount of Mg would lead to  $S'$  phase coalescing to coarse lath morphology, which exerts deleterious influence on the mechanical properties [6,14]. Several researchers demonstrated that the L1<sub>2</sub>-structured Al<sub>3</sub>(Sc,Zr) particles introduced by Sc addition could also play an important role in dispersing the coplanar caused by  $\delta'$ (Al<sub>3</sub>Li) phase, resulting in the significant enhancement of ductility and

strength [7,15,16]. Moreover, Sc could greatly refine the grain size and effectively inhibit the coarsening of  $\delta'$ -precipitating free zones (PFZs) [7]. An excellent combination of high strength (yield strength of 408 MPa and ultimate tensile strength of 491 MPa) and ductility (elongation of 6.0%) was obtained in permanent mold cast Al–2Li–2Cu–0.5Mg–0.2Sc–0.2Zr alloy suffered to the heat treatment of (480 °C, 32 h) + (540 °C, 24 h) + (175 °C, 32 h) [17].

Due to the large solidification interval of high Li-containing Al–Li–Cu alloys, permanent mold cast Al–Li alloys will make uncontrollable hot cracks in some mass and complex components. Compared with permanent mold cast, the sand cast is superior in some cases because of its deformability which can reduce the tendency of hot cracking. Nevertheless, SAIKAWA et al [18] found that the ultimate tensile strength and elongation of sand cast 8091 alloys in T4 and T6 conditions were much lower than those of the permanent casting method. The problem can be solved by optimizing the heat treatment process, but there is little research on it. It is demanded to fill the gap of improving the heat treatment scheme to modify the microstructures, precipitation sequences and mechanical properties of sand cast Al–Li–Cu alloys.

Based on the previous study of ZHANG et al [17], the sand cast Al–2Li–2Cu–0.5Mg–0.2Sc–0.2Zr alloy was selected to study the effect of heat treatment schemes on the microstructure and mechanical properties. The content of Li in the studied alloy was high and this work might provide a comprehensive understanding of the precipitate interactions and precipitation behaviors to the high Li-containing sand cast Al–Li–Cu–Mg alloys.

## 2 Experimental

The Al–2Li–2Cu–0.5Mg–0.2Sc–0.2Zr alloy in this work was prepared from master alloys of Al–10%Zr, Al–50%Cu and commercially pure Al, Mg and Li. The specifics of the melting procedures have been detailed elsewhere [19]. Chemical analysis was exerted by inductively couple plasma-atomic emission spectroscopy (ICP-AES), and the result is listed in Table 1. Differential scanning calorimetry (DSC, SAT449F3) was

carried out on the as-cast samples employing a constant heating rate of 10 °C/min for assisting the solution treatment scheme design. Combining the result of DSC, three-stage solution treatment schemes ((460 °C, 32 h) + (520 °C, 24 h) + (530/540/550 °C, 4/12/24/32 h)) were designed to sufficiently dissolve the secondary phases into the matrix. After quenching into cold water following solution treatments, the specimens were aged at 125, 175, and 225 °C for various periods ranging from 0 to 1024 h in an oil bath.

**Table 1** ICP component results of sand cast Al–2Li–2Cu–0.5Mg–0.2Sc–0.2Zr alloy (wt.%)

Li	Cu	Mg	Sc	Zr	Fe	Al
2.10	2.08	0.54	0.19	0.21	0.026	Bal.

Optical micrograph (OM) and scanning electron microscope (SEM) samples were mechanically ground on SiC papers from 500 to 7000 grit, followed by polishing on MgO waster solution wetted cloth. Polished specimens were etched by Keller's reagent (5 mL HNO<sub>3</sub>, 3 mL HCl, 2 mL HF and 190 mL distilled water) for 20 s before observation. The microstructures were observed on optical microscope (LEICAMEF4M) and scanning electron microscope (SEM, Phenom XL). Energy dispersive spectroscopy (EDS) and X-ray diffraction (XRD, Ultima IV) were employed for phase analysis. The area fraction of the secondary phases and average diameter of grain sizes were measured by Image-Pro-Plus image analysis software.

During the artificial aging, Vickers hardness tests were carried out on polished samples using a load of 5 kg and a dwell time of 15 s. Tensile tests of sheet specimens were performed at room temperature utilizing Zwick/Roell Z100 equipped with a non-contact extensometer at a strain rate of 1.0 mm/min. Each result was determined as the average of five texts. Thin foils for the transmission electron microscopy (TEM) examinations were prepared by the twin-jet electropolishing method using a 4 vol.% perchloric acid and 96 vol.% ethanol solution cooled down to approximately –30 °C. TEM observation was carried out by a JEM2100 microscope (JEOL Ltd.) operated at 200 kV.

### 3 Results and discussion

#### 3.1 Microstructure of as-cast alloy

Figure 1 presents the XRD pattern of sand cast Al–2Li–2Cu–0.5Mg–0.2Sc–0.2Zr alloy in the as-cast state. The peaks from  $\alpha(\text{Al})$ ,  $\delta'(\text{Al}_3\text{Li})$ ,  $\delta(\text{AlLi})$ ,  $\theta'(\text{Al}_2\text{Cu})$ ,  $\text{Al}_3\text{Sc}$ ,  $T_2(\text{Al}_6\text{CuLi}_3)$  and  $T_1(\text{Al}_2\text{CuLi})$  phases can be observed in the spectrum, which is the same as the result of the permanent mold cast alloy [17]. Moreover, no diffraction peaks related to  $\text{Al}_2\text{MgLi}$  and  $\text{Al}_{7.5}\text{Cu}_4\text{Li}$  phases were found, possibly due to their small contents. Thus, it can be speculated that the lower cooling rate did not change the phase constitutions in the sand cast alloy.

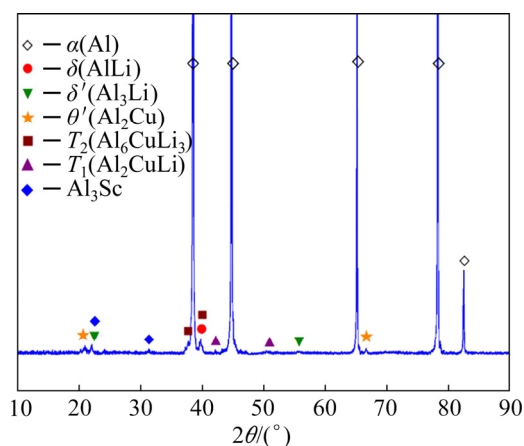


**Fig. 1** XRD pattern of sand cast Al–2Li–2Cu–0.5Mg–0.2Sc–0.2Zr alloy in as-cast state

The OM image of sand cast Al–2Li–2Cu–0.5Mg–0.2Sc–0.2Zr alloy in the as-cast state is illustrated in Fig. 2(a). As a contrast, the result of metal mold casting is exhibited in Fig. 2(b). The results showed that there existed severe dendritic segregation and high content of secondary phases along the grain boundary or in interdendritic regions in the sand cast alloy. Comparatively, equiaxed grains were dominated in the permanent mold cast alloy. According to the measurements, the average grain size (GS) of the sand cast alloy was about 66.43  $\mu\text{m}$  and the area fraction ( $f_A$ ) of intermetallic compounds is about 9.6%, while those of the permanent mold cast alloy were about 30.49  $\mu\text{m}$  and 2.7%, respectively. Owing to the low cooling rate, the solidification rate of the sand cast alloy was limited and the grain size of the sand cast alloy was larger than that of the permanent mold

cast alloy [13]. Moreover, the lower cooling rate caused a higher driving force for the formation of the secondary phases and prolonged the period of the eutectic reaction, leading to a larger area fraction of the secondary phases [14].

Figures 2(c–h) display the SEM backscattered micrograph and the corresponding element distributions acquired by EDS of the sand cast alloy. Element Cu was greatly enriched in the coarse secondary phases distributing along the grain boundaries or interdendritic regions for its high solute partitioning coefficient [15–17]. The transition elements Sc and Zr were observed to segregate in some regions, which might form  $\text{Al}_3\text{Sc}$  and  $\text{Al}_3\text{Zr}$  primary phases. While the distribution of element Li could not be detected due to its small atomic number.

#### 3.2 Microstructure and mechanical properties after solution heat treatments

The DSC results of the sand cast Al–2Li–2Cu–0.5Mg–0.2Zr–0.2Sc alloy in the as-cast and quenched states are presented in Fig. 3. It can be observed that there were two endothermic peaks *A*, *C* and one exothermic peak *B*. Peak *A* at around 100  $^{\circ}\text{C}$  was attributed to the dissolution of  $\delta'(\text{Al}_3\text{Li})$  phase [20]. Peak *B* near 300  $^{\circ}\text{C}$  was due to the precipitation of  $\delta$ ,  $S'$  and  $T_1$  phases [21]. Peak *C* located at 543.2  $^{\circ}\text{C}$  was representative of the melting and dissolution of Cu-bearing secondary phases [6]. The addition of Cu, Mg and Li might form  $\text{Al}_2\text{Cu}$ ,  $T_1$ ,  $\text{Al}_2\text{CuMg}$  and  $T_2$  phases. According to Al–Cu binary phase diagram [22], the eutectic melting temperature of  $\text{Al}_2\text{Cu}$  phase was 548.2  $^{\circ}\text{C}$ , which approached the temperature of Peak *C*. No detection of several separate endothermic peaks related to  $\text{Al}_2\text{CuLi}$  and  $\text{Al}_2\text{CuMg}$  phases was possibly attributed to their low volumes. There were no melting peaks of the  $\text{Al}_3\text{Sc}$  and  $\text{Al}_3\text{Zr}$  phases that appeared before the  $\alpha(\text{Al})$  matrix was melted at about 650  $^{\circ}\text{C}$  for their high melting temperatures [23,24].

In principle, the solvus temperature represents the temperature capable of maximizing the dissolution of secondary phases, which should be lower than the solidus temperature. After suffering to (460  $^{\circ}\text{C}$ , 32 h) + (520  $^{\circ}\text{C}$ , 24 h) two-stage heat treatment [17], which was designed for permanent mold cast Al–2Li–2Cu–0.5Mg–0.2Zr–0.2Sc alloy, representative OM and SEM backscattered images

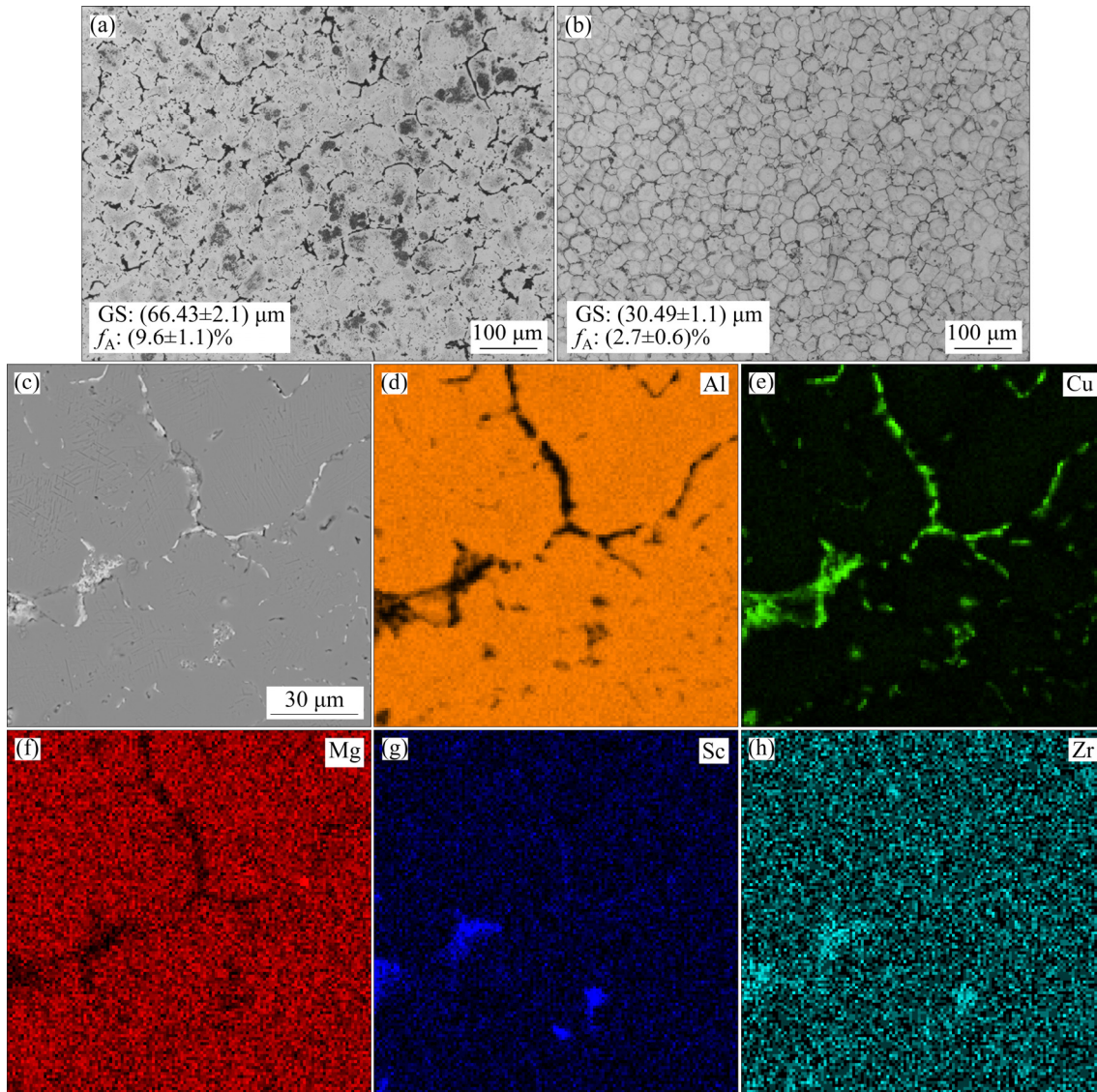


**Fig. 2** Microstructures of sand cast and metal cast Al-2Li-2Cu-0.5Mg-0.2Sc-0.2Zr alloys in as-cast state: (a) OM image of sand cast alloy; (b) OM image of metal cast alloy; (c) SEM backscattered micrograph of sand cast alloy; (d) Element map-scanning of Al; (e) Element map-scanning of Cu; (f) Element map-scanning of Mg; (g) Element map-scanning of Sc; (h) Element map-scanning of Zr

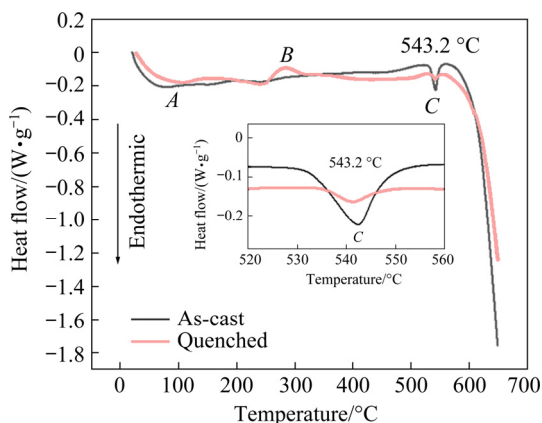


**Fig. 3** DSC curves of sand cast Al-2Li-2Cu-0.5Mg-0.2Sc-0.2Zr alloy in as-cast and quenched states

of the sand cast and permanent mold cast alloys are illustrated in Fig. 4. There still existed high content of residual secondary phases in the sand cast alloy ( $f_A$  was about 5.5%), as shown in Fig. 4(a). The EDS mapping result of the sand cast alloy suffered to the two-stage heat treatment is illustrated in Figs. 4(d–h), showing the undissolved secondary phases along grain boundaries, which were harmful to the mechanical properties. Comparatively, most of the secondary phases in the permanent mold cast alloy were almost dissolved into the matrix and the average area fraction of residual phases was only 0.2%, as shown in Fig. 4(b).

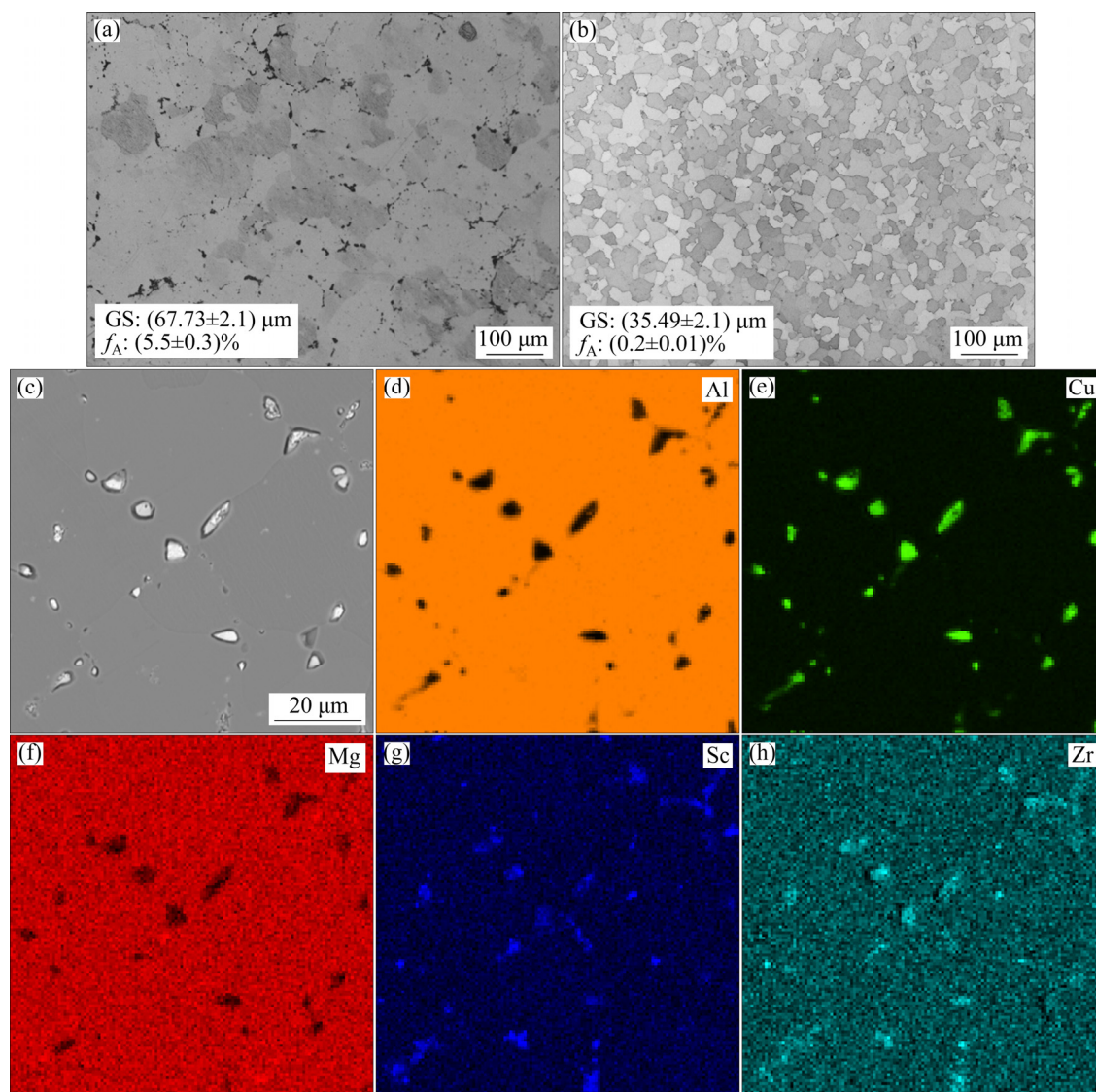


**Fig. 4** Microstructures of sand cast and metal cast Al-2Li-2Cu-0.5Mg-0.2Sc-0.2Zr alloys after (460 °C, 32 h) + (520 °C, 24 h) two-stage solution treatment: (a) OM image of sand cast alloy; (b) OM image of metal cast alloy; (c) SEM backscattered micrograph of sand cast alloy; (d) Element map-scanning of Al; (e) Element map-scanning of Cu; (f) Element map-scanning of Mg; (g) Element map-scanning of Sc; (h) Element map-scanning of Zr

To dissolve the residual secondary phases more completely, one more stage at a higher temperature was demanded to enhance the diffusion rates of Cu, Sc and Zr atoms. Three solution temperatures (530, 540 and 550 °C) for the third stage were studied in this work. The OM images of the sand cast Al-2Li-2Cu-0.5Mg-0.2Sc-0.2Zr under different conditions ((460 °C, 32 h) + (520 °C, 24 h) + (530/540/550 °C, 4/12/24/32 h)) are exhibited in Fig. 5. When the temperature of the third stage was 530 °C, the  $f_A$  of eutectics gradually reduced from 5.5% to the lowest value of 3.6% with the period of the third stage increasing from 4 to 12 h. After the third stage was

further prolonged to 32 h, there was no obvious reduction in the content of residual phases. When the temperature increased to 540 and 550 °C, obviously overburnt microstructures of melting compounds at some trifurcate grain boundaries were discovered as indicated by the red circles shown in Figs. 5(f, i, k, l), which would significantly damage the mechanical properties [25]. Meanwhile, the increase of grain size was slightly inhibited as the solution temperature elevated and time prolonged due to the pinning effect of the residual phases [26].

The SEM backscattered micrographs of the quenched sand cast and permanent mold cast

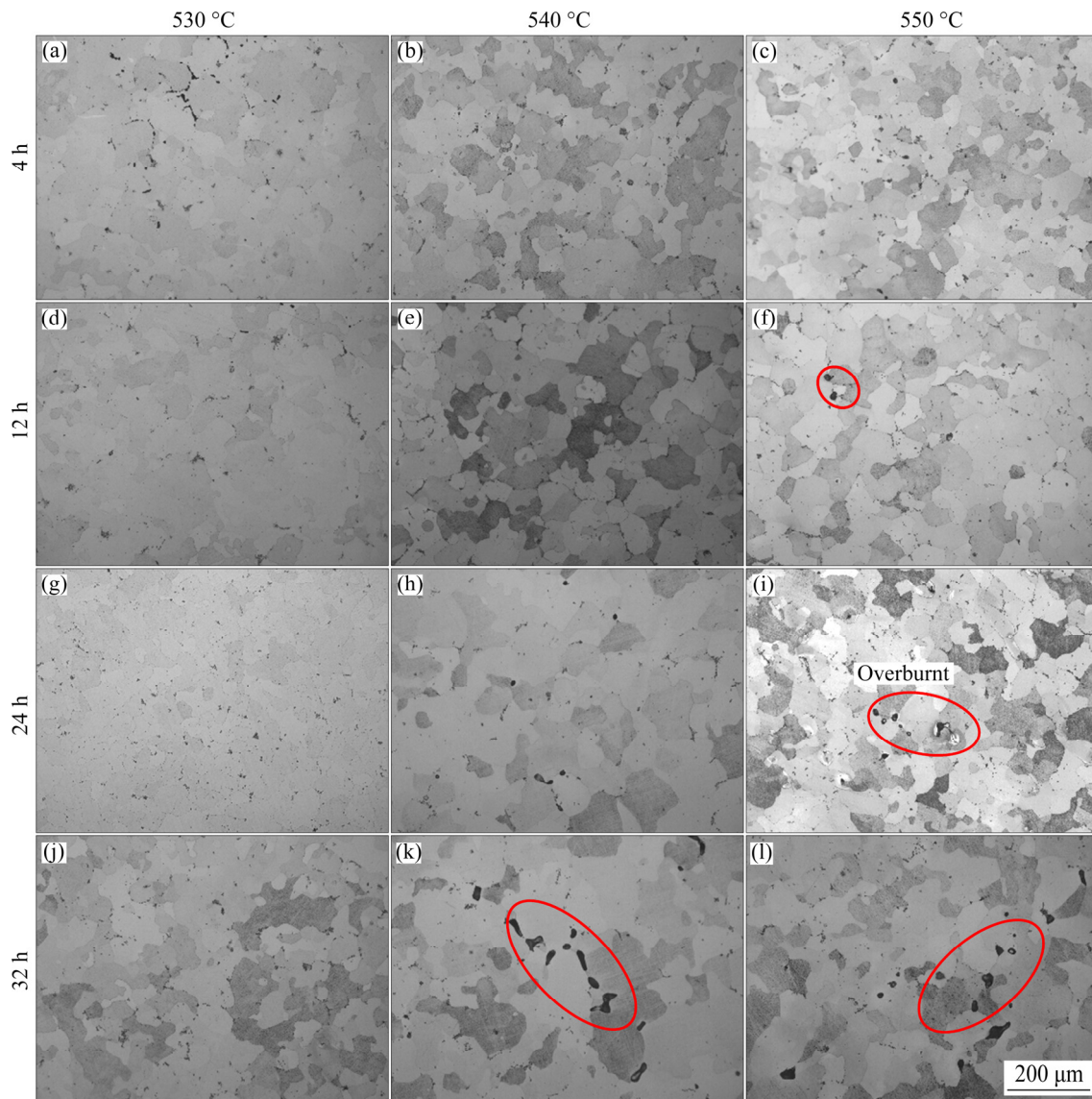


**Fig. 5** OM images of alloy under solution treatment conditions of (460 °C, 32 h) + (520 °C, 24 h) + (530/540/550 °C, 4/12/24/32 h)

Al–2Li–2Cu–0.5Mg–0.2Sc–0.2Zr alloys after optimal solution treatments are presented in Fig. 6. After the three-stage solution treatment scheme ((460 °C, 32 h) + (520 °C, 24 h) + (530 °C, 12 h)), the content of residual secondary phases in sand cast alloy was much lower than that in Fig. 4(a). However, compared with the permanent mold cast alloy suffered to (460 °C, 32 h) + (520 °C, 24 h) two-stage heat treatment, the content of residual phases of the sand cast alloy suffered to the optimal three-stage solution treatment was still a bit high. The  $f_A$  of the secondary phases in the quenched sand cast alloy is about 1.6%, while it is only about 0.2% in the quenched permanent mold cast alloy. From the sand cast result shown in Fig. 3, it can be

found that the endothermic peak of the Cu-containing phases in the quenched sand cast alloy still appeared, indicating that a small amount of residual Cu-bearing phases were hard to be dissolved.

The mechanical properties of sand cast Al–2Li–2Cu–0.5Mg–0.2Sc–0.2Zr alloy suffered to (460 °C, 32 h) + (520 °C, 24 h) + (530 °C, 4/12/24/32 h) are illustrated in Fig. 7. As the third stage prolonged from 4 to 12 h, the YS, EL and UTS increased by 24 MPa, 3.5% and 40 MPa, respectively. The enhancement can be concluded as the synergic influence of solution strengthening and dissolution of the secondary phases [27]. However, all the mechanical properties values kept decreasing

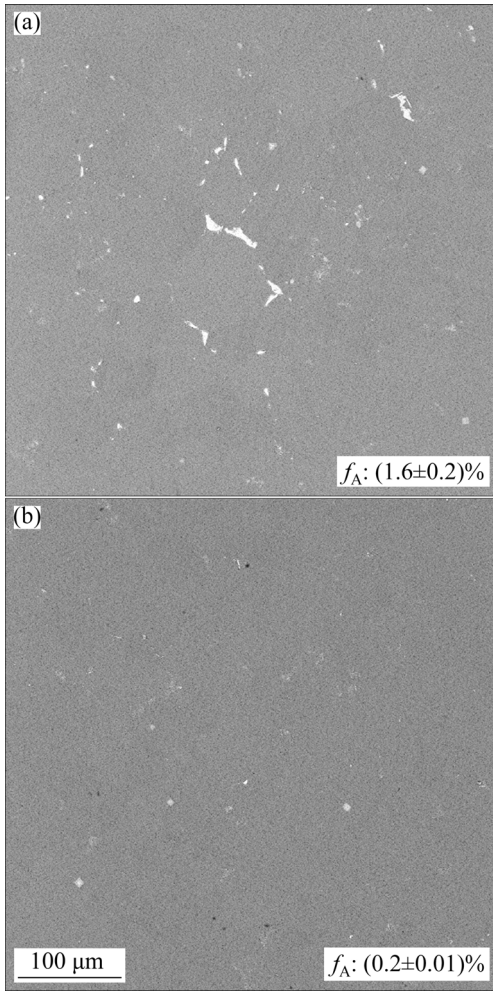


**Fig. 6** SEM backscattered micrographs of sand cast and permanent mold cast Al-2Li-2Cu-0.5Mg-0.2Sc-0.2Zr alloys in quenched state: (a) Sand cast alloy after solution treatment of (460 °C, 32 h) + (520 °C, 24 h) + (530 °C, 12 h); (b) Permanent mold cast alloy after solution treatment of (460 °C, 32 h) + (520 °C, 24 h)

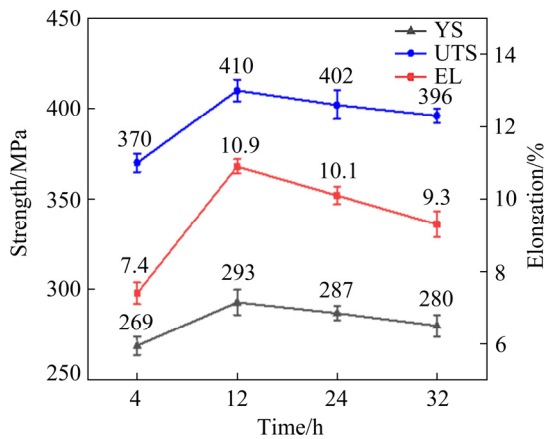


**Fig. 7** Mechanical properties of sand cast Al-2Li-2Cu-0.5Mg-0.2Sc-0.2Zr alloy under solution treatment of (460 °C, 32 h) + (520 °C, 24 h) + (530 °C, 4/12/24/32 h)

gradually with the third stage further prolonging, which might be attributed to the coarsening of grains but without further dissolution of residual secondary phases, as shown in Fig. 5. The sand cast Al-2Li-2Cu-0.5Mg-0.2Sc-0.2Zr alloy could obtain a good combination of strength (YS=293 MPa, UTS=410 MPa), and ductility (EL=10.9%) suffered to the solution treatment of (460 °C, 32 h) + (520 °C, 24 h) + (530 °C, 12 h), which was therefore the optimal scheme. Most of the secondary phases were dissolved into the matrix and a smaller grain size (75.21 μm) was obtained.

### 3.3 Mechanical properties after aging

Following the optimal solution treatment, the sand cast Al-2Li-2Cu-0.5Mg-0.2Sc-0.2Zr alloy suffered to artificial aging at 125, 175 and 225 °C, respectively. Figure 8 shows the aging hardening curves as a function of the aging time. The studied alloy possessed strong age-hardening responses at all temperatures, while the periods required for reaching peak-aged state dramatically decreased as the aging temperatures elevated. Especially, the specimen aged at 125 °C even could not reach the peak-aged value until 1000 h. The highest hardness of HV 175.6 was obtained in the sample aged at 175 °C for 64 h. Comparatively, permanent mold cast alloy obtained the highest hardness of HV 184 after 175 °C aging for 32 h [17], indicating that the permanent mold cast alloy has a stronger age-hardening response. When aged at 225 °C, the hardness increased rapidly and reached a peak value of HV 145.3 at 4 h, followed by a continuous decrease as the aging time prolonged.

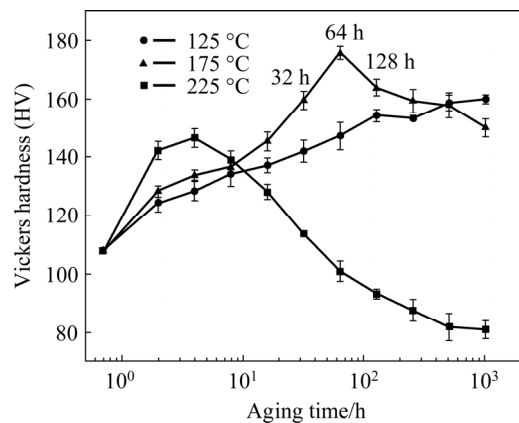


**Fig. 8** Aging hardening curves of sand cast Al-2Li-2Cu-0.5Mg-0.2Sc-0.2Zr alloy in quenched state at different temperatures

The aging response speed of 125 °C was too low to be suitable for practical application, while the 225 °C aging temperature was thought to cause heterogeneous distribution of  $\delta'$  phase and weaken the mechanical properties [7,28–30]. A detailed microstructure analysis will be exerted. Thus, only the samples aged at 175 °C were selected for the tensile test, which was also exerted in the permanent mold cast alloy [17].

The mechanical properties of the sand cast alloy in different conditions, including solution treated (ST), under-aged state (UA, aged at 175 °C for 8 h), peak-aged state (PA, aged at 175 °C for 64 h) and over-aged state (OA, aged at 175 °C for 128 h), are shown in Fig. 9. As the artificial aging proceeded, there was a significant improvement in YS and UTS, accompanied by an apparent reduction in ductility from the quenched state to UA and PA states. When the aging time was prolonged to 128 h (OA), the YS and UTS turned to decrease while the elongation was slightly enhanced. After aging at 175 °C for 8 h, excellent comprehensive mechanical properties of YS=376 MPa, UTS=458 MPa and EL=4.1% were obtained.

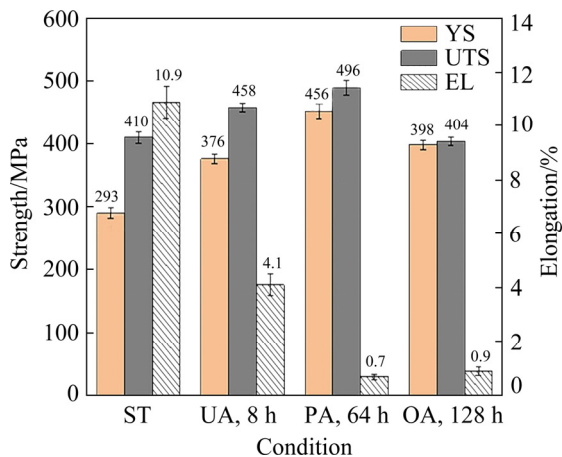


**Fig. 9** Mechanical properties of sand cast alloy at different states, including solution treatment and aging at 175 °C for varying time

Compared with permanent mold cast alloy [17], there existed a similar variation trend of strength and ductility of sand cast alloy with the increase of aging time. However, under the peak aging condition, the strength and elongation of sand cast alloy were both lower than those of permanent mold cast alloy. As shown in Fig. 4, the grain size of sand cast alloy was much larger than that of permanent mold cast alloy, which was one of the

reasons that accounted for its lower mechanical properties. According to the Hall–Petch relationship ( $\Delta\sigma_{gb}=k_{Al}d^{-0.5}$ ,  $\Delta\sigma_{gb}$  is the increment of the yield stress at the grain boundary caused by the grain refinement;  $d$  is the grain size, and  $k_{Al}=0.15 \text{ MPa}\cdot\text{m}^{-0.5}$ ), the contribution from grain refining was only about 3 MPa (66  $\mu\text{m}$  of sand cast alloy and 30  $\mu\text{m}$  of permanent mold cast alloy). Thus, the precipitation behavior, which was speculated to bring about a great effect on the mechanical properties of the sand cast alloy, should be investigated.

### 3.4 Microstructure and precipitation evolution during aging

Figure 10 presents the  $L1_2$ -centred dark-field (DF) images of the sand cast samples aged at different states. The  $L1_2$ -structured  $\delta'$  phase has a superlattice structure with a lattice parameter of  $a=0.405 \text{ nm}$  and the orientation relationship with the matrix is  $(100)_{\delta'}/(100)_{Al}$  and  $[001]_{\delta'}/[001]_{Al}$  [29,31]. The metastable  $\delta'$  phase is the predominant precipitation phase in high Li-containing (>1.7 wt.%) Al–Li–Cu alloys [29]. Because of the ordered  $\text{Cu}_3\text{Au}$  crystal structure of  $\delta'$  and the presence of paired dislocations in aged Al–Li alloys, the strengthening imparted by  $\delta'$  phases is mainly attributed to the order-hardening mechanism [32]. Moreover, the continuous precipitation and coarsening of  $\delta'$  phases resulted in strength enhancement and severe toughness reduction because of the coplanar slipping [33].

As shown in Figs. 10(a–c), it can be found that the spherical  $\delta'$  particles, accompanied by some  $\text{Al}_3(\text{Zr},\text{Sc},\text{Li})$  composite precipitates, were homogeneously distributed in the matrix of the samples aged at 125 and 175 °C. The generally non-shearable  $\text{Al}_3(\text{Zr},\text{Sc})$  cores, serving as preferring nucleation sites for  $\delta'$  [34], are expected to be highly resistant to dislocations shear. The average diameter of the  $\delta'$  phase aged at 175 °C increased obviously, whilst the coarsening rate of the  $\delta'$  phase aged at 125 °C was extremely low, as shown in Figs. 10(a–c). Nevertheless, the morphology of the  $\delta'$  phase was heterogeneous under 225 °C aging, as shown in Fig. 10(d). It can be explained that the kinetics of the coarsening of  $\delta'$ , which obeys Ostwald ripening, is a diffusion-controlled process, as solute atoms are transferred through the matrix from the shrinking precipitates to the growing

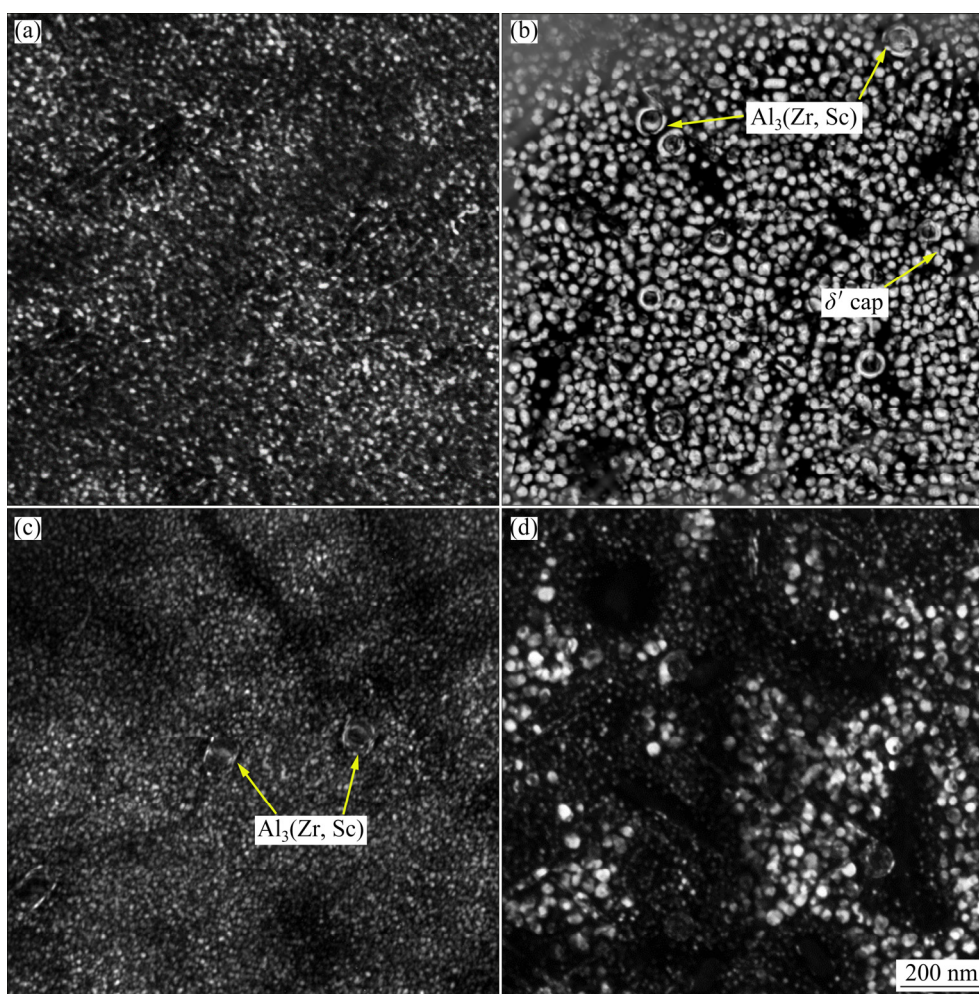


**Fig. 10**  $L_{12}$ -centered DF TEM images of sand cast alloy in different aging states: (a) Aged at 175 °C for 8 h; (b) Aged at 175 °C for 64 h; (c) Aged at 125 °C for 128 h; (d) Aged at 225 °C for 4 h

ones [35,36]. Therefore, if the aging temperature is elevated to 225 °C, the competition relationship of the particles will be intensified greatly, resulting in uneven morphology. The extremely fine  $\delta'$  under 125 °C aging had a limited strengthening effect and the heterogeneous distribution of the  $\delta'$  aged at 225 °C was harmful to the ductility. Because the precipitation of  $\delta'$  is predominant in the high Li-bearing systems, the homogeneous and ripened  $\delta'$  in the matrix aged at 175 °C was one of the important reasons for the high strength.

Figures 11(a, b) show the BF TEM images of the sand cast alloy aged at 175 °C for 8 and 64 h, respectively. The amount and size of lath-shaped  $S'$  precipitate increase under 175 °C aging, accompanied by serendipitous  $T_1$  plates. There were only some  $Al_3(Zr, Sc)$  particles surrounded by dislocations that could be found in the matrix aged at 125 °C for 128 h, as presented in Fig. 11(c). The  $T_1$  phase is predominant and the average size is

about 300 nm after aging at 225 °C for only 4 h, which is much bigger than that in the sample aged at 175 °C. Combined with the result of permanent mold cast alloy [17], it can be concluded that the precipitation evolution is temperature-dependent rather than the casting methods. Since there is low content of dislocations serving as nucleation sites for  $T_1$ , the precipitation of  $T_1$  in as-cast Al–Li–Cu alloys is mainly dependent on the helical dislocations or loops formed by the annihilation of the vacancies retained by quenching [37]. Therefore, as the aging temperature was elevated to 225 °C, a large number of free vacancies were released by the Li-vacancy to form  $\delta'$  and evolved into the loops for  $T_1$  nucleation. The precipitation sequence of  $S'$  dominated in the matrix of the sample aged at 175 °C because of the high Mg–Cu–vacancy binding energy [38]. Due to the elevated temperature of the third solution stage, there existed a high content of vacancies in the quenched sand

cast alloy, leading to more nucleation sites for Cu-containing phases and a higher strengthening effect. Therefore, the sand cast alloy showed an extremely high strength after aging at 175 °C for 64 h.

Figures 12 (a, b) show the  $\delta'$ -precipitating free zones (PFZs) of the sand cast alloy aged at 175 °C in UA and PA states. The average half-width of the PFZs increased from 18 to 169 nm as aging time prolonged from 8 to 64 h. The formation and

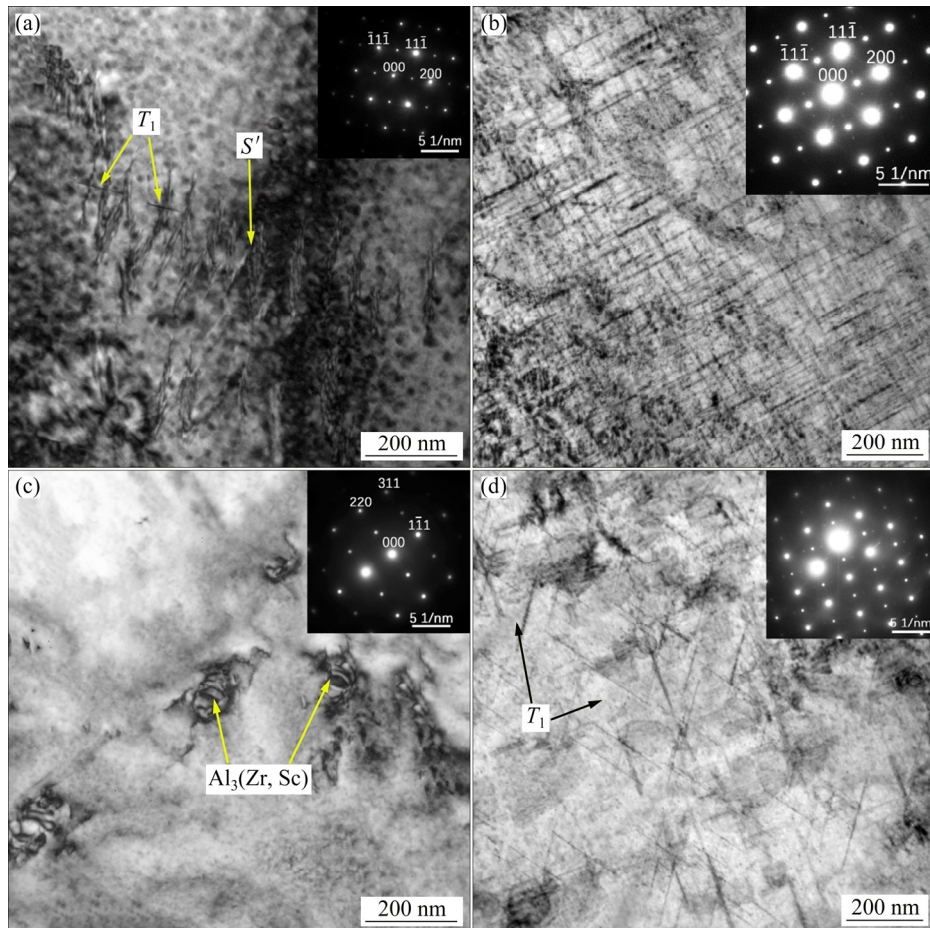


**Fig. 11** BF TEM images of sand cast alloy in different aging states: (a) Aged at 175 °C for 8 h; (b) Aged at 175 °C for 64 h; (c) Aged at 125 °C for 128 h; (d) Aged at 225 °C for 4 h

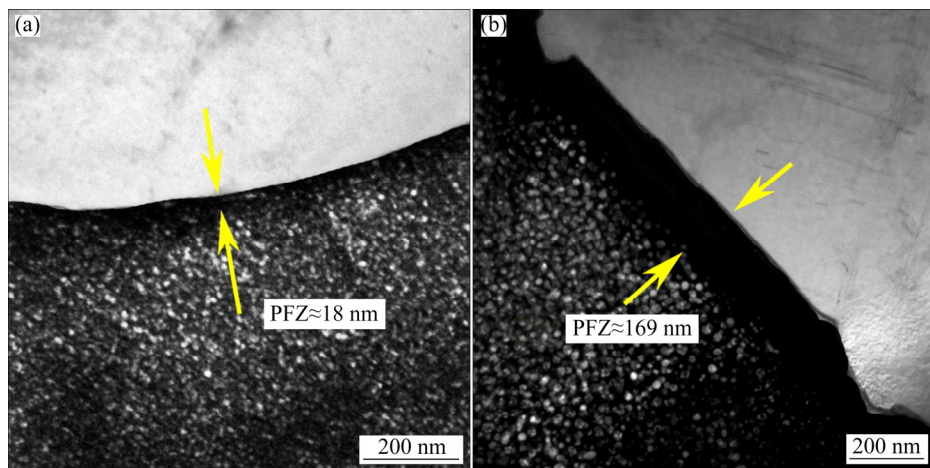


**Fig. 12**  $\delta'$  centered dark-field images near grain boundaries of sand cast alloy aged at 175 °C for different time: (a) 8 h; (b) 64 h

growth of  $\delta'$ -PFZs have been interpreted as the result of the growth of equilibrium phase  $\delta$ (AlLi) consuming the Li atoms from  $\delta'$  at grain boundaries, where the diffusion coefficient of Li was high [30]. The formation and coarsening of the soft  $\delta'$ -PFZs, in which the stress concentration and microcracks preferentially occur, reduce the ductility of the as-cast Al–Cu–Li alloy [7]. Compared with the permanent mold cast alloy [17], the half-width of  $\delta'$ -PFZs in the sand cast alloy increased by about 102% at the PA state. It is widely accepted that the coarsening of  $\delta'$ -PFZs followed a parabolic growth law expressed by

$$h=K_p t^{0.5}$$

where  $h$  is the half-width of  $\delta'$ -PFZs,  $t$  is the aging time and  $K_p$  is the  $\delta'$ -PFZs growth rate constant. Despite the time needed for reaching PA of sand cast alloy is twice that of permanent mold cast alloy, the growth rate constant  $K_p$  is also higher. This might be due to the higher content of vacancies caused by the third stage of solution treatment, resulting in higher atom diffusion rates during aging. And the residual secondary phases along with grain boundaries might also provide more lattice defects, which could serve as nucleation sites for  $\delta$  phase.

Three EDS points of the fracture surface of the studied alloy in the UA state are shown in Fig. 13. It shows an intergranular fracture morphology and there are Cu, Sc, and Zr elements enriched at Points 2 and 3. The residual secondary phases are speculated to induce microcracks during deformation. Thus, the higher content of residual

phases and wider  $\delta'$ -PFZs in the sand cast alloy than those in permanent mold cast alloy led to a much lower elongation. Modifying the grain boundaries is the key to enhancing the ductility, which might be controlled by several factors involving the microalloying, further improving the heat treatment scheme and higher cooling rate during solidification. It will be the subject of our subsequent research.

## 4 Conclusions

(1) Owing to the low cooling rate, the sand cast Al–2Li–2Cu–0.5Mg–0.2Sc–0.2Zr alloy obtained a large average grain size and high area fraction of secondary phases. After the improved solution treatment scheme of (460 °C, 32 h) + (520 °C, 24 h) + (530 °C, 12 h), the content of residual secondary phases was decreased.

(2) An augmented area fraction of the  $S'$  phase precipitated during aging, accompanied by some  $T_1$  phase and  $Al_3(Zr,Sc,Li)$  particles when aging at 175 °C. Meanwhile, the  $\delta'$  ( $Al_3Li$ ) phase homogeneously precipitated and grew, resulting in a great enhancement of strength. The other two aging temperatures of 125 and 225 °C were not suitable for modifying the microstructure.

(3) As aging prolonged, the high coarsening rate of  $\delta'$ -PFZs resulted in a great reduction of elongation. The combination of larger grains, wider  $\delta'$ -PFZs and more residual secondary phases in the sand cast alloy was responsible for the worse ductility compared with those of the permanent mold cast alloy.

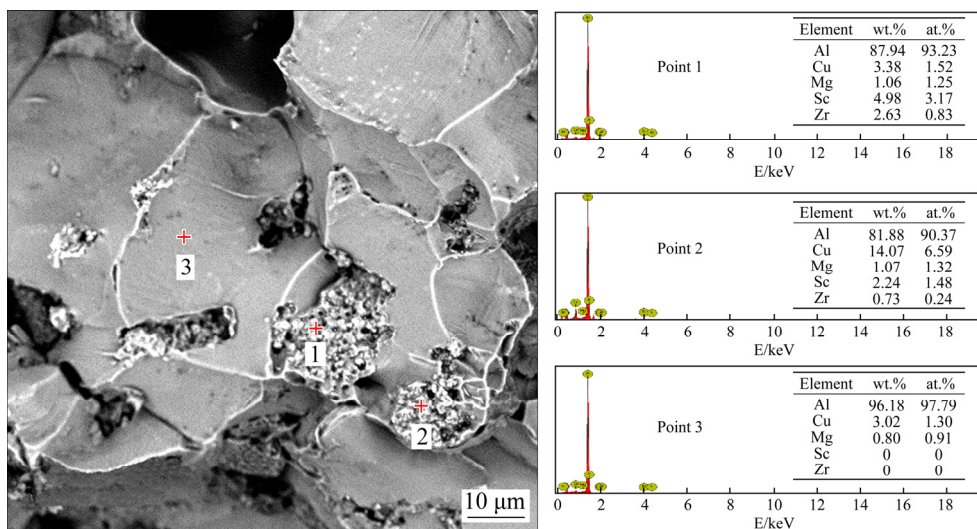


**Fig. 13** Fracture surface and EDS results of sand cast Al–2Li–2Cu–0.5Mg–0.2Sc–0.2Zr alloy aged at 175 °C for 8 h in UA state

(4) After aging at 175 °C for 8 h, good comprehensive mechanical properties of UTS=376 MPa, YS=458 MPa and EL=4.1% were obtained.

## Acknowledgments

This work was financially supported by the National Natural Science Foundation of China (Nos. 51871148, 51821001) and the United Fund of National Department of Education and Equipment Development, China (No. 6141A02033245).

## References

- [1] RIOJA R J, JOHN J. The evolution of Al–Li base products for aerospace and space applications [J]. *Metallurgical and Materials Transactions A*, 2012, 43: 3325–3337.
- [2] VELAGIN I, ZAKHAROV V V. Modern Al–Li alloys and prospects of their development [J]. *Metal Science & Heat Treatment*, 2013, 55: 184–190.
- [3] LU Ding-ding, LI Jin-feng, HONG Ning, MA Peng-cheng, CHEN Yong-lai, ZHANG Xu-hu, ZHANG Kai, LI Jian-mei, ZHANG Rui-feng. Effects of microstructure on tensile properties of AA2050-T84 Al–Li alloy [J]. *Transactions of Nonferrous Metals Society of China*, 2021, 31: 1189–1204.
- [4] JATA K V, HOPKINS A K, RIOJA R J. The anisotropy and texture of Al–Li alloys [J]. *Materials Science Forum*, 1996, 217–222: 647–652.
- [5] GREGSON P, FLOWER H. Microstructural control of toughness in aluminum–lithium alloys [J]. *Acta Metallurgica*, 1985, 33: 527–537.
- [6] ZHANG Xiao-long, ZHANG Liang, WU Guo-hua, SHI Chun-chang, ZHANG Jin-shuo. Influences of Mg content on the microstructures and mechanical properties of cast Al–2Li–2Cu–0.2Zr alloy [J]. *Journal of Materials Science*, 2019, 54: 791–811.
- [7] ZHANG Jin-shuo, WU Guo-hua, ZHANG Liang, ZHANG Xiao-long, SHI Chun-chang, TONG Xin. Addressing the strength–ductility trade-off in a cast Al–Li–Cu alloy—Synergistic effect of Sc-alloying and optimized artificial aging scheme [J]. *Journal of Materials Science & Technology*, 2022, 96: 212–225.
- [8] ZHANG Jin-shuo, WU Guo-hua, ZHANG Liang, ZHANG Xiao-long, SHI Chun-chang, SUN Jiang-wei. Effect of Zn on precipitation evolution and mechanical properties of a high strength cast Al–Li–Cu alloy [J]. *Materials Characterization*, 2020, 160: 110089.
- [9] GUMBMANN E, LEFEBVRE W, GEUSER D F, SIGLI C, DESCHAMPS A. The effect of minor solute additions on the precipitation path of an Al–Cu–Li alloy [J]. *Acta Materialia*, 2016, 115: 104–114.
- [10] MEDJAHED A, HENNICHE A, DERRADJI M, YU T F, WANG Y, WU R Z, HOU L G, ZHANG J H, LI X L, ZHANG M L. Effects of Cu/Mg ratio on the microstructure, mechanical and corrosion properties of Al–Li–Cu–Mg–X alloys [J]. *Materials Science and Engineering A*, 2018, 718: 241–249.
- [11] GUMBMANN E, GEUSER F D, SIGLI C, DESCHAMPS A. Influence of Mg, Ag and Zn minor solute additions on the precipitation kinetics and strengthening of an Al–Cu–Li alloy [J]. *Acta Materialia*, 2017, 133: 172–185.
- [12] HUANG J C, ARDELL A J. Crystal structure and stability of  $T_1$  precipitates in aged Al–Li–Cu alloys [J]. *Metal Science Journal*, 2013, 3: 176–188.
- [13] GUPTA A K, GAUNT P, CHATURVEDI M C. The crystallography and morphology of the  $S'$ -phase precipitate in an Al(CuMg) alloy [J]. *Philosophical Magazine*, 1987, 55: 375–387.
- [14] HU Ze-yi, FAN Cai-he, SHEN Tong, OU Ling, DAI Nan-shan, WANG Lu. Effect of aging treatment on evolution of  $S'$  phase in rapid cold punched Al–Cu–Mg alloy [J]. *Transactions of Nonferrous Metals Society of China*, 2021, 31: 1930–1938.
- [15] MA Juan, YAN De-sheng, RONG Li-jian, LI Yi-yi. Effect of Sc addition on microstructure and mechanical properties of 1460 alloy [J]. *Acta Metallurgica Sinica*, 2014, 24: 13–18.
- [16] SINGH V, PRASAD K S, GOKHALE A A. Effect of minor Sc additions on structure, age hardening and tensile properties of aluminium alloy AA8090 plate [J]. *Scripta Materialia*, 2004, 50: 903–908.
- [17] ZHANG Xiao-long, ZHANG Liang, WU Guo-hua, SUN Jiang-wei, RONG Mian, HSIEH C C, YU Yu-xiang. Influence of Sc content on the microstructure and mechanical properties of cast Al–2Li–2Cu–0.5Mg–0.2Zr alloy [J]. *Materials Characterization*, 2018, 142: 223–236.
- [18] SAIKAWA S, SUGIOKA S, NAKAI K, SUGIURA Y, KAMIO A. Microstructure and mechanical properties of 8091 Al–Li alloys cast into permanent and sand molds [J]. *Journal of Japan Institute of Light Metals*, 1995, 45: 261–266.
- [19] ZHANG Xiao-long, ZHANG Liang, WU Guo-hua, LIU Wen-cai, SHI Chun-chang, TAO Jia-shen. Microstructural evolution and mechanical properties of cast Al–2Li–2Cu–0.5Mg–0.2Zr alloy during heat treatment [J]. *Materials Characterization*, 2017, 132: 312–319.
- [20] GHOSH K S, DAS K, CHATTERJEE U K. Studies of retrogression and reaging behavior in a 1441 Al–Li–Cu–Mg–Zr alloy [J]. *Metallurgical & Materials Transactions A*, 2005, 36: 3477–3487.
- [21] LUO A, LLOYD D J, GUPTA A, YOUDELIS W V. Precipitation and dissolution kinetics in Al–Li–Cu–Mg alloy 8090 [J]. *Acta Metallurgica et Materialia*, 1993, 41: 769–776.
- [22] CHEN S W, CHANG Y A. Application of thermodynamic models to the calculation of solidification paths of Al-rich Al–Li alloys [J]. *Metallurgical Transactions A*, 1991, 22: 267–271.
- [23] KANG Y B, PELTON A D, CHARTRAND P, FUERST C D. Critical evaluation and thermodynamic optimization of the Al–Ce, Al–Y, Al–Sc and Mg–Sc binary systems [J]. *Calphad*, 2008, 32: 413–422.
- [24] OKAMOTO H. The Al–Zr (aluminum–zirconium) system [J]. *Journal of Phase Equilibria*, 2002, 23: 455–456.
- [25] LI Hong-ying, SU Xiong-jie, YIN Hao, HUANG De-sheng. Microstructural evolution during homogenization of

- Al–Cu–Li–Mn–Zr–Ti alloy [J]. Transactions of Nonferrous Metals Society of China, 2013, 23: 2543–2550.
- [26] PENG Yu, CHEN An-tao, ZHANG Liang, LIU Wen-cai, WU Guo-hua. Effect of solution treatment on microstructure and mechanical properties of cast Al–3Li–1.5Cu–0.2Zr alloy [J]. Journal of Materials Research, 2016, 8: 1–9.
- [27] ZHANG Fei, SHEN Jian, YAN Xiao-dong, SUN Jian-li, SUN Xiao-long, YANG Yin. Homogenization heat treatment of 2099 Al–Li alloy [J]. Rare Metals, 2014, 33: 28–36.
- [28] GU B P, LIEDL G L, KULWICKI J H, SANDERS T H Jr. Coarsening of  $\delta'$ (Al<sub>3</sub>Li) precipitates in an Al–2.8Li–0.3Mn alloy [J]. Materials Science and Engineering, 1985, 70: 217–228.
- [29] WILLIAMS D B, EDINGTON J W. The precipitation of  $\delta'$ (Al<sub>3</sub>Li) in dilute aluminium–lithium alloys [J]. Metal Science, 1975, 9: 529–532.
- [30] JHA S C, SANDERS T H Jr, DAYANANDA M A. Grain boundary precipitate free zones in Al–Li alloys [J]. Acta Metallurgica, 1987, 35: 473–482.
- [31] KEKKINGTON S H, LOVERIDGE D, TITMAN J M. Research notes: The lattice parameters of some alloys of lithium [J]. Journal of Physics D: Applied Physics, 1969, 2: 1162–1163.
- [32] HUANG J C, ARDELL A J. Precipitation strengthening of binary Al–Li alloys by  $\delta'$  precipitates [J]. Materials Science and Engineering A, 1988, 104: 149–156.
- [33] STARINK M J, HOBSON A J, SINCLAIR I, GREGSON P J. Embrittlement of Al–Li–Cu–Mg alloys at slightly elevated temperatures: Microstructural mechanisms of hardening [J]. Materials Science and Engineering A, 2000, 289: 130–142.
- [34] TERRONES L, MONTEIRO S N. Composite precipitates in a commercial Al–Li–Cu–Mg–Zr alloy [J]. Materials Characterization, 2007, 58: 156–161.
- [35] FLOWER H M, GREGSON P J. Solid state phase transformations in aluminium alloys containing lithium [J]. Materials Science and Technology, 1987, 3: 81–90.
- [36] PÉREZ-LANDEZÁBAL J I, NÓ M L, MADARIAGA G, RECARTE V, JUAN J S. Quantitative analysis of  $\delta'$  precipitation kinetics in Al–Li alloys [J]. Acta Materialia, 2000, 48: 1283–1296.
- [37] NOBEL B, THOMPSON G E.  $T_1$ (Al<sub>2</sub>CuLi) precipitation in aluminium–copper–lithium alloys [J]. Metal Science Journal, 1972, 6: 167–174.
- [38] PENG J, BAHL S, SHYAM A, HAYNES J A, SHIN D. Solute–vacancy clustering in aluminum [J]. Acta Materialia, 2020, 196: 747–758.

## 热处理工艺对砂型铸造 Al–2Li–2Cu–0.5Mg–0.2Sc–0.2Zr 合金显微组织和力学性能的影响

张晋硕, 钟晓祥, 张亮, 吴国华, 刘文才

上海交通大学 材料科学与工程学院 轻合金精密成型国家工程研究中心

金属基复合材料国家重点实验室, 上海 200240

**摘要:** 研究不同热处理工艺对砂型铸造 Al–2Li–2Cu–0.5Mg–0.2Sc–0.2Zr 合金显微组织和力学性能的影响。设计三级固溶处理方案((460 °C, 32 h) + (520 °C, 24 h) + (530/540/550 °C, 4/12/24/32 h))和不同温度(125, 175, 225 °C)时效处理方案用于比较。采用光学显微镜(OM)、扫描电子显微镜(SEM)和透射电子显微镜(TEM)分析显微组织演变过程。结果表明, 最佳固溶处理((460 °C, 32 h) + (520 °C, 24 h) + (530 °C, 12 h))可溶解大部分晶界第二相。透射电镜结果表明, 经 175 °C 时效 8 h 后,  $\delta'$ (Al<sub>3</sub>Li)颗粒均匀分布于基体中, 并伴有少量板条状  $S'$ (Al<sub>2</sub>CuMg)和片状  $T_1$ (Al<sub>2</sub>CuLi)相。采用最佳热处理方案((460 °C, 32 h) + (520 °C, 24 h) + (530 °C, 12 h) + (175 °C, 8 h))可获得屈服强度为 376 MPa、极限抗拉强度为 458 MPa 和伸长率为 4.1%的最佳综合性能。

**关键词:** Al–Li–Cu 合金; 砂型铸造; 热处理; 析出相; 显微组织; 力学性能

(Edited by Wei-ping CHEN)